42nd AIAA Aerospace Sciences Meeting and Exhibit
5 - 8 January 2004, Reno, Nevada

AIAA 2004-0157

Multi-Scale Modeling for LES of Engineering Designs of Large-Scale Combustors

S. Menon, C. Stone and N. Patel
School of Aerospace Engineering
Georgia Institute of Technology
Atlanta, Georgia 30332

42nd Aerospace Sciences Meeting and Exhibit
January 5–8, 2004 / Reno, NV

Multi-Scale Modeling for LES of Engineering Designs of Large-Scale Combustors

S. Menon*, C. Stone †and N. Patel ‡
School of Aerospace Engineering
Georgia Institute of Technology
Atlanta, Georgia 30332

Lean-Blowout (LBO) is a phenomenon that occurs in both land-based premixed and propulsion liquid-fuelled gas turbine engines when the effective equivalence ratio is reduced close to the lean flammability limit. Small perturbations in the flame or flow can result in local quenching that can subsequently lead to total extinction (LBO). Large and sudden increase in CO emission is known to follow local quenching near LBO. Prediction of pollutant emission and combustion dynamics near LBO is very complicated since physics at many interacting scales have to be resolved. In this study, LES using a subgrid linear-eddy mixing (LEM) model is used in both premixed and liquid-fuelled gas turbine engines to determine if this type of LES can predict not only the flame structure but also pollutant emission. In the premixed study, comparison is made with a thin-flame approach and it is shown that the flame length can be changed drastically by adjusting the parameters in the flame speed model used in the thin-flame approach, whereas the flame length is actually predicted in the subgrid LEM approach. It is also shown that oxidation of UHC in the post-flame zone and local quenching have to be included to obtain the proper CO emission trend (as observed in data) near LBO. Results of LES in a full-scale liquid-fuelled gas turbine are also discussed in this context using both heptane and kerosene finite-rate kinetics mechanism. Conditions of low and full power are simulated and analyzed.

1 INTRODUCTION

Gas turbines for power generation operate in the lean premixed mode since this mode of combustion reduces the flame temperature and decreases considerably the amount of pollutants (CO and NO) formed at the flame front. However, as the reactant equivalence ratio decreases and the combustion process approaches the lean flammability limit, the combustion process and the flame become susceptible to small perturbations inside the combustion chamber. These perturbations manifest themselves as pressure oscillations and perturb the fuel feeding system causing spatial inhomogeneity in the incoming reactant mixture. These in-homogeneities can modify the heat release pattern, which in turn, can trigger new pressure fluctuations.[1] Unsteady heat release in-phase with the pressure oscillation can lead to large-amplitude pressure oscillation, often called combustion instability.

Combustion instability in gas turbine engines is a major problem in general, but more so in the lean limit. Perturbation in heat release can (and does) lead to local and/or total flame extinction. Combustion instability, if it occurs, can accelerate this flame extinction process. LBO can occur with or without accompanying combustion instability depending upon the combustor design and operating conditions. The equivalence ratio at which LBO occurs is larger than the lean flammability limit and depends upon the mixture properties, as well as on the geometry, heat loss, level of turbulence, etc.

LBO has been observed not only in premixed systems but also in liquid fueled combustors and thus, is a generally observed feature in practical combustors. Experimental studies show that an exponential increase in CO emission level occurs in the vicinity of the LBO limit.[2] Although the exact process behind this phenomenon is not well understood, it is likely due to local quenching of the flame in the highly turbulent regions, which releases unburned hydrocarbons (UHC) into the post flame region that subsequently oxidize into CO. In liquid-fuelled systems, physics near LBO is probably effected also by droplet vaporization and mixing effects. Predicting this phenomenon, as well as predicting engine performance near LBO, is currently a major research effort.

In this study, we report on LES studies of combustion near LBO in both premixed and liquid-fueled systems. We study two combustors: a US Department of Energy combustor (called DOE-HAT, hereafter) and a representative liquid-fueled combustor developed at General Electric[3] (called GE-1, hereafter). The operating condition near LBO needs to be properly resolved in order to achieve accurate prediction. For example, in premixed system when the Karlovitz number, defined as $Ka = \delta_F/\eta$ (where δ_F is the laminar flame thickness and η is the Kolmogorov scale)

*Professor, Associate Fellow
†Research Engineer
‡Graduate Assistant, Student Member

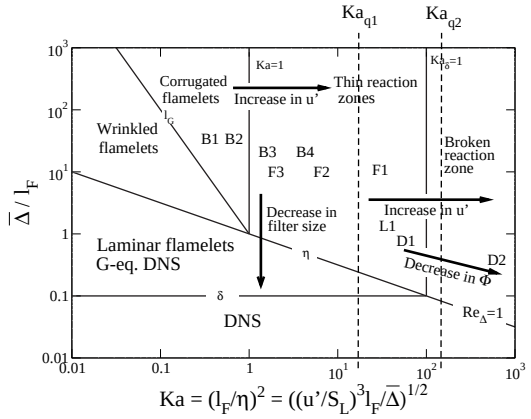

Fig. 1 Premixed combustion regimes[5] and locations of typical flames: B-type ([6]), F-type ([7]), General Electric LM-6000 ([4]) (L1) and the current DOE-HAT combustor (D1 for Φ>0.6 and D2 for Φ<0.5). Here, Φ is the equivalence ratio, l_F is the flame thickness, u' the sub-grid velocity fluctuations, S_L the laminar flame speed and $\overline{\Delta}$ is the grid size.

is smaller than 100, turbulent structures do not penetrate the reaction zone. The flames in the flamelet and Thin-Reaction-Zone (TRZ) regimes exhibit this feature. In both these regimes, the flame surface (identified by the thin-reaction region) and its propagation can be tracked accurately using computationally efficient level-set methods such as the G-equation approach.[4,5] As the turbulence level increases, such that $Ka > 100$, the smaller turbulent structures can penetrate into the reaction zone and modify its structure. This regime is often called the Broken-Reaction-Zone (BRZ) regime since the typical concept of a single connected flame is no longer applicable. In such a highly turbulent regime, local flame extinction (and hence, re-ignition) is expected and needs to be included.

As shown in Fig. 1, typical operating condition in full-scale premixed gas turbine engines falls in the TRZ regime and as the mixture becomes lean, the operating condition enters the BRZ regime. In contrast, most laboratory flames are in the corrugated flamelet or well within the TRZ regime. Thus, for proper prediction of flame extinction and combustion dynamics near LBO, the LES approach must be able to deal with changes in flame structure from the TRZ to the BRZ regimes without requiring ad hoc changes in the model. In spray combustion system, these issues are still relevant since combustion can occur simultaneously in premixed, partially premixed and non-premixed mode due to complex interaction between droplet motion, vaporization and fuel-air mixing in such combustors.

This paper describes a comprehensive simulation method that has the potential to address all regimes of combustion in premixed and in liquid-fueled engines without requiring any ad hoc model adjustment. Furthermore, with proper inclusion of reaction kinetics, this approach can also predict pollutant emission. We describe the subgrid mixing and combustion model called the linear-eddy mixing (LEM) model[8,9] in LES with a particular focus on its application to combustion near the LBO limit. Past studies[10,11,12,13] have shown that the LEM model can handle combustion under a wide range of conditions and thus, is considered a natural candidate for the present applications.

2 FORMULATION

In this section, we briefly describe the formulation of the LES model in order to establish the methodology used in the current study. More details are given in cited references.

2.1 LES Equations

The governing equation of motion for an unsteady, compressible, reacting, multi-species fluid are employed in this study. Compressible model is essential in order to capture the coupling between pressure oscillations (acoustic wave motion), vorticity dynamics and combustion heat release that is expected to occur near LBO. Using a Favre filtering approach, the LES equations can be derived. The details are given elsewhere and therefore, avoided here, for brevity.[14,13]

In this section, governing equations and the modeling techniques used in LES are presented. The flow variables are decomposed into the resolved (super-grid scale) and unresolved (sub-grid scale) components by a spatial filtering operation, such that $f = \tilde{f} + f"$, where the tilde ($\sim$) denotes resolved scale and double prime (") denotes unresolved sub-grid scale quantities. The Favre filtered variable is defined as $\tilde{f} = \overline{\rho f}/\bar{\rho}$ where the over-bar represents a spatial filtering.

Applying the filtering operator to the conservation equations of mass momentum, energy and species equations results in the following LES equations for two-phase flows:

$$\begin{aligned}
\frac{\partial \bar{\rho}}{\partial t} &+ \frac{\partial \bar{\rho}\tilde{u}_i}{\partial x_i} = 0 \\
\frac{\partial \bar{\rho}\tilde{u}_i}{\partial t} &+ \frac{\partial}{\partial x_j}[\bar{\rho}\tilde{u}_i\tilde{u}_j + \bar{p}\delta_{ij} - \bar{\tau}_{ij} + \tau^{sgs}_{ij}] = 0 \\
\frac{\partial \bar{\rho}\tilde{E}}{\partial t} &+ \frac{\partial}{\partial x_i}[(\bar{\rho}\tilde{E} + \bar{p})\tilde{u}_i + \bar{q}_i - \tilde{u}_j\bar{\tau}_{ji} + H^{sgs}_i + \sigma^{sgs}_i] = 0 \\
\frac{\partial \bar{\rho}\tilde{Y}_k}{\partial t} &+ \frac{\partial}{\partial x_i}[\bar{\rho}\tilde{Y}_k\tilde{u}_i - \bar{\rho}\tilde{Y}_k\widetilde{V_{i,k}} + Y^{sgs}_{i,k} + \theta^{sgs}_{i,k}] = \bar{\dot{w}}_k
\end{aligned}$$

where $k = 1$ to N_s and N_s is the total number of species present in the system. $\bar{q}_i$ is the heat flux vector given by

$$\bar{q}_i = -\bar{\kappa}\frac{\partial \tilde{T}}{\partial x_i} + \bar{\rho}\sum_{k=1}^{N_s}\tilde{h}_k\tilde{Y}_k\widetilde{V_{i,k}} + \sum_{k=1}^{N_s} q^{sgs}_{i,k} \qquad (1)$$

The diffusion velocities are approximated using Fickian diffusion as $\widetilde{V_{i,k}} = (-\bar{D}_k/\tilde{Y}_k)(\partial\tilde{Y}_k/\partial x_i)$. The subgrid terms that require closure are:

$$\tau^{sgs}_{ij} = \bar{\rho}\,(\widetilde{u_i u_j} - \tilde{u}_i\tilde{u}_j)$$

$$
\begin{aligned}
H_i^{sgs} &= \bar{\rho}\,(\widetilde{Eu_i} - \widetilde{E}\widetilde{u}_i) + (\overline{pu_i} - \bar{p}\widetilde{u}_i) \\
\sigma_i^{sgs} &= \widetilde{u_j\tau_{ij}} - \widetilde{u}_j\overline{\tau}_{ij}. \\
Y_{i,k}^{sgs} &= \bar{\rho}[\widetilde{u_iY_k} - \tilde{u}_i\tilde{Y}_k] \\
q_{i,k}^{sgs} &= [\overline{h_kD_k\partial Y_k/\partial x_i} - \tilde{h}_k\tilde{D}_k\partial\tilde{Y}_k/\partial x_i] \\
\theta_{i,k}^{sgs} &= \bar{\rho}[\widetilde{V_{i,k}Y_k} - \widetilde{V}_{i,k}\widetilde{Y}_k]
\end{aligned}
\tag{2}
$$

The pressure is determined from the filtered equation of state, $\bar{p} = \bar{\rho}R\tilde{T} + T^{sgs}$. Here, T^{sgs} is the temperature-species correlation term, defined as $[\widetilde{Y_kT} - \tilde{Y}_k\tilde{T}]$. For low heat-release, T^{sgs} can be expected to be negligible[15] but this may not be true for high heat release. However, due to the difficulty in modeling these terms they are generally neglected.[15] Note that in the LEMLES method discussed here, this term can be explicitly computed from the LEM field and can be included without any closure.

The filtered total energy per unit volume is given by $\bar{\rho}\tilde{E} = \bar{\rho}\tilde{e} + \frac{1}{2}\bar{\rho}\tilde{u}_i\tilde{u}_i + \bar{\rho}k^{sgs}$ where, the sub-grid kinetic energy (to be discussed later) is defined as, $k^{sgs} = (1/2)[\widetilde{u_ku_k} - \tilde{u}_k\tilde{u}_k]$. The filtered internal energy for calorically perfect gases is given by

$$
\tilde{e} = \sum_{k=1}^{N_s}[c_{v,k}\tilde{Y}_k\tilde{T} + \tilde{Y}_k\Delta h_{f,k}^{'}] \tag{3}
$$

where, $\Delta h_{f,k}^{'} = \Delta h_{f,k}^0 - c_{p,k}T^0$ and $\Delta h_{f,k}^0$ is the standard heat of formation at a reference temperature T^0.

2.2 Momentum Closure

Model for sub-grid stress tensor τ_{ij}^{sgs} is derived usually by drawing an analogy between the viscous stresses, (τ_{ij}) in the unfiltered Navier-Stokes equation and the sub-grid stresses, (τ_{ij}^{sgs}) in the filtered equations. Hence, the deviatoric part of the sub-grid stresses is assumed to be proportional to the deviatoric part of the resolved rate of strain, $\tilde{S_{ij}} = (1/2)(\partial\tilde{u}_i/\partial x_j + \partial\tilde{u}_j/\partial x_i)$. If the sub-grid stress tensor can be split into deviatoric and isotropic parts $\tau_{ij}^{sgs} = \tau_{ij,d}^{sgs} + \tau_{kk}^{sgs}$, then the deviatoric part $\tau_{ij,d}^{sgs}$, is modeled as follows;

$$
\tau_{ij,d}^{sgs} = -2\bar{\rho}\nu_t[\tilde{S_{ij}} - \frac{1}{3}\tilde{S_{kk}}\delta_{ij}] \tag{4}
$$

Noting that $\tau_{kk}^{sgs} = (2/3)\bar{\rho}k^{sgs}\delta_{ij}$, the total sub-grid stress tensor can be expressed as

$$
\tau_{ij}^{sgs} = -2\bar{\rho}\nu_t[\tilde{S_{ij}} - \frac{1}{3}\tilde{S_{kk}}\delta_{ij}] + \frac{2}{3}\bar{\rho}k^{sgs}\delta_{ij} \tag{5}
$$

Therefore, to complete the closure for the sub-grid stresses, the sub-grid eddy viscosity ν_t and the sub-grid kinetic energy, k^{sgs} need to be modeled.

A non-equilibrium model[16,17] using a transport equation for the sub-grid kinetic energy, k^{sgs} is used in this study and is given by :

$$
\frac{\partial\bar{\rho}k^{sgs}}{\partial t} + \frac{\partial}{\partial x_i}\left(\bar{\rho}\tilde{u}_ik^{sgs}\right) = P^{sgs} - \epsilon^{sgs} + \frac{\partial}{\partial x_i}\left(\bar{\rho}\frac{\nu_t}{Pr_t}\frac{\partial k^{sgs}}{\partial x_i}\right) \tag{6}
$$

The terms, P^{sgs} and ϵ^{sgs} in the above equation are respectively, production and dissipation of sub-grid kinetic energy. The sub-grid dissipation, ϵ^{sgs} is obtained by integrating the dissipation spectrum $(D(k) = -2\nu k^2E(k))$ over the unresolved wavenumbers,[11] to get

$$
\epsilon^{sgs} = C_\epsilon\bar{\rho}(k^{sgs})^{3/2}/\overline{\Delta} \tag{7}
$$

where, $C_\epsilon = 0.916$. The sub-grid production term is modeled as $P^{sgs} = -\tau_{ij}^{sgs}(\partial\widetilde{u}_i/\partial x_j)$. The coefficient Pr_t is the turbulent Prandtl number and is taken to be 0.9. The sub-grid eddy viscosity is modeled as[11]

$$
\nu_t = 0.067\sqrt{k^{sgs}}\Delta \tag{8}
$$

The coefficients 0.067 (in the expression for ν_t) and 0.916 (in the expression for ϵ^{sgs}) can also be obtained as a part of the solution by using the dynamical procedure, as shown earlier.[14] More information on dynamic modeling can be found elsewhere.[14,18]

2.3 Scalar Transport Closure

In addition to τ_{ij}^{sgs}, several unclosed terms appear in the LES filtered energy and species equations given in Eqn. (2), such as:

$$
\begin{aligned}
H_i^{sgs} &- \text{sub-grid enthalpy flux} \\
\sigma_i^{sgs} &- \text{sub-grid viscous work} \\
Y_{i,k}^{sgs} &- \text{convective species flux} \\
q_{i,k}^{sgs} &- \text{sub-grid heat flux} \\
\theta_{i,k}^{sgs} &- \text{sub-grid species diffusive flux}
\end{aligned}
\tag{9}
$$

The sub-grid total enthalpy flux H_i^{sgs} is also modeled using the eddy viscosity model as follows:

$$
H_i^{sgs} = \frac{-\bar{\rho}\nu_t}{Pr_t}\frac{\partial\tilde{H}_k}{\partial x_i}
$$

Note that, since large-scale motion is resolved in LES, the associated counter-gradient processes in the resolved scales are also resolved (even though a gradient closure is employed for H_i^{sgs}). The other unclosed terms like σ_i^{sgs}, $q_{i,k}^{sgs}$ and $\theta_{i,k}^{sgs}$, are often neglected and there exists no model for these terms. These terms are the sub-grid contribution of the molecular diffusive flux and are often neglected assuming that their contributions are small in high Reynolds number flows.[15]

The sub-grid convective species flux $Y_{i,k}^{sgs}$, given in equation Eqn. [2] is modeled using the gradient diffusion assumption as follows.

$$
Y_{i,k}^{sgs} = \frac{-\bar{\rho}\nu_t}{Sc_t}\frac{\partial\tilde{Y}_k}{\partial x_i}
$$

The coefficient Sc_t is the turbulent Schmidt Number, and is taken to be unity. Nevertheless, theory and experiments have shown that this gradient diffusion

assumption for species transport can lead to significant errors.

Most of these assumptions for neglecting the sub-grid terms such as $q_{i,k}^{sgs}$ and $\theta_{i,k}^{sgs}$, and the gradient diffusion modeling for $Y_{i,k}^{sgs}$ are often not justifiable. In the LES-LEM approach (to be described in the next section), most of these assumptions can be relaxed and can be elegantly included in the model for sub-grid scalar transport.

2.4 Subgrid Scalar Closure

The LEM model of Kerstein *et al*[19] is used in the LES approach. In LEMLES, all the physical processes such as molecular diffusion, small and large scale turbulent convection and chemical reaction are modeled separately, but concurrently at their respective time scales. This multi-scale phenomena is solved using a two-scale numerical approach.

Consider the transport equation for a scalar ψ and split the velocity field according to the LES technique: $u = \widetilde{u} + u'$.

$$\frac{\partial \psi}{\partial t} = -\widetilde{u_k}\frac{\partial \psi}{\partial x_k} - u_k'\frac{\partial \psi}{\partial x_k} + \frac{\partial}{\partial x_m}\left[D_\psi \frac{\partial \psi}{\partial x_m}\right] + w_\psi \quad (10)$$

where D_ψ is the molecular diffusion coefficient and w_ψ is the chemical reaction source term. In LEMLES, the two-scale numerical procedure is represented as:

$$\frac{\psi^* - \psi^n}{\Delta t_{LES}} = -\widetilde{u_k}\frac{\partial \psi}{\partial x_k} - \left(u_k'\right)^{face}\frac{\partial \psi}{\partial x_k} \quad (11)$$

$$\psi^{n+1} - \psi^n = \int_t^{t+\Delta t_{LES}} \left[u_k'\frac{\partial \psi}{\partial x_k} + \frac{\partial}{\partial x_m}\left(D_\psi \frac{\partial \psi}{\partial x_m}\right) + w_\psi\right] dt \quad (12)$$

Equation 11 describes the large-scale 3D LES-resolved convection of the scalar field and is implemented via the transfer of fluid volumes between LES control volumes through the control volume surfaces. The convection by the term $\left(u_k'\right)^{face}$ is the convection of the scalars through the control volume surfaces due to the sub-grid velocity field. Equation 12 describes the sub-grid stirring, via $\int_t^{t+\Delta t_{LES}} u_k'\frac{\partial \psi}{\partial x_k} dt$ and the subgrid molecular diffusion and reaction kinetics that occur within each LES cell.

Since the sub-grid resolution is assumed sufficient to resolve all scales below the LES grid scale, reaction and diffusion processes are included in an exact manner within the 1D domain. This closure is similar to the closure in PDF methods[20] except that unlike in PDF methods, molecular diffusion (and hence, differential diffusion) effects can also be included in LEMLES. As in PDF methods, the large-scale transport (Eq. 11) is modeled as a Lagrangian transport of the scalar fields across LES cells and the sub-grid turbulent stirring is modeled (in Eq. 12). In PDF methods, the Curl's coalescence-dispersion mixing model is often employed to model turbulent mixing, whereas in LEMLES, small-scale turbulent stirring is implemented using a scalar rearrangement process that mimics the action of an eddy upon the scalar field.[19] The location of this stirring event is chosen from a uniform distribution and the frequency of stirring is derived from 3D inertial range scaling laws derived from Kolmogorov's hypothesis as:

$$\lambda = \frac{54}{5}\frac{\nu Re_{\overline{\Delta}}}{C_\lambda \overline{\Delta}^3}\frac{[(\overline{\Delta}/\eta)^{5/3} - 1]}{[1 - (\eta/\overline{\Delta})^{4/3}]} \quad (13)$$

C_λ represent the scalar turbulent diffusivity and is determined as 0.067. The eddy size (l) is chosen from the following PDF:

$$f(l) = \frac{(5/3)l^{-8/3}}{\eta^{-5/3} - \overline{\Delta}^{-5/3}} \quad (14)$$

where $\eta = N_\eta \overline{\Delta} Re_{\overline{\Delta}}^{-4/3}$. The empirical constant N_η reduces the effective range of scale between the integral length scale and η but does not change the turbulent diffusivity ($N_\eta \in [1.3;10.78]$).

It has been demonstrated that the turbulent scaling laws predict correctly the growth of the flame surface area under the influence of turbulent strain. Note that, this model does not require any change when the flame type (premixed or diffusion flame) or the combustion regime (flamelet, TRZ or BRZ regimes) changes. This ability has been demonstrated in the past[12,21] and it is this ability that we believe is crucial to deal with complex phenomenon such as LBO. Further details are given in cited references and therefore, avoided here for brevity.

Conservation of mass, momentum and energy (at the LES level) and conservation of mass, energy and species (at the LEM level) are strongly coupled.[13] Chemical reaction at the LEM level determines heat release and thermal expansion at the LEM level, which at the LES level generates flow motion that, in turns, transports the species field at the LEM level. Full coupling is maintained in the LEMLES to ensure local mass conservation.

2.5 Combustion Modeling

Combustion and heat release are governed by chemical kinetics and influenced by turbulence. In premixed system, chemical heat release is modeled using two different approaches. In the first approach a level set approach is used, where the premixed flame front is represented by an infinitely thin surface that is convected by the flow and propagates normal to itself at a characteristic flame speed S_T. This model (called GLES hereafter) is referred as the G-Equation model.[22] Although very cost effective, GLES requires a model for the turbulent flame speed, $S_T = S_T(u', S_L)$, to close the GLES equation. A flame speed model $S_T = S_L(1 + \beta(u'/S_L)^2)^{1/2}$ (which

has been calibrated in high Φ flamelet combustion for a fixed range of $u'/{S_L}^4$) is used here. As the mixture becomes leaner, S_L decreases and so u'/S_L becomes very large in regions with high turbulence. However, in reality for high value of u'/S_L, S_T/S_L actually bends toward 0 since the flame will eventually go extinct due to stretch effects.[22] Therefore, the typical flame length and structure predicted by this type of model is likely to be non-physical in high $u'S_L$ regions.

The second approach (called LEMLES hereafter) uses a simplified five species, 1-step Arrhenius rate law. For methane-air combustion in the DOE-HAT combustor, a 5-species/1-step mechanism:[23]

$$CH_4 + 2(O_2 + 3.76N_2) \rightleftharpoons CO_2 + 2H_2O + 7.52N_2 \quad (15)$$

is used. In the liquid-fueled system we study heptane-air kinetics using a similar 1-step global mechanism and kerosene-air kinetics using a three-step, 8-species mechanism.[3] The latter mechanism includes models for CO and NO, in addition to UHC (the unburned fuel) and thus, can be used to predict pollutant emission.

In LES it is necessary to predict the filtered reaction rate $\bar{\dot{w}}_k$. When implemented in a conventional closure, a subgrid Eddy Break-Up model (SEBU) is employed.[24] However, in LEMLES, no closure is needed since the exact reaction-diffusion processes are simulated within each LES cell. To accelerate the computation of chemistry evaluation in LEMLES we employ a ISAT[25] technique to speed up the chemistry computation. Parallel implementation of the subgrid LEM model also enhances the overall operational speed of the code.

In the present premixed study using the 1-step mechanism, CO and NO emission are modeled in the LES using an approach developed earlier[26] and thus, in both GLES and LEMLES, the same pollutant model is employed.[27,21] In the liquid fueled system no emission (other than UHC) is included in the heptane-air case and only preliminary results are currently available on emission data for the kerosene-air case, and thus, only discussed qualitatively. Simulations are still underway to investigate emission in the kerosene-air case.

3 NUMERICAL IMPLEMENTATION

3.1 DOE-HAT Geometry and Operating Conditions

The geometry of the DOE-HAT combustor is shown in Fig. 2 (a). In this combustor, the premixed mixture enters the combustor in a swirling manner through a circular slot. The flame is stabilized by the recirculation in the base of the dump and also by the recirculation created by the center body. The length of the combustion chamber is 0.5 m, its radius is 0.053 m and the inlet is located between 0.0173 m and 0.0314 m from the centerline. The length of the combustor is chosen so that the emissions predictions (which is only available at 0.381 m from the dump plane) can be computed and compared with data.

The inflow characteristics are chosen as given in the earlier DOE-HAT experiment: the fuel is methane (CH_4) and the reactants enter the combustor with a temperature of 700 K, a pressure of 1.378 MPa., and a mean inflow velocity of 68.6 m/s. The flow is swirling and the swirl number is 0.6. The Reynolds number based on the inlet velocity and the diameter of the center-body is 230,000. A random turbulent field is added to the inflow mean velocity and a sub-grid turbulence intensity of around 7 percent is used to specify the incoming sub-grid kinetic energy. Characteristic based inflow and outflow boundary conditions are employed for all the reported simulations.

3.2 GE-1 Geometry and Operating Conditions

The conditions for the GE-1 are chosen similar to those reported earlier[3] and represents two possible operating conditions: Case 1: pilot only (start-up) and Case 2: pilot and main (full power). The chosen conditions represent realistic operation of this complex engine. As shown in Fig. 3 this configuration consists of two cups with multiple swirlers within a sector. Figure 4 shows the inflow velocity profiles employed in each swirl cup. Since there is no proper characterization of the inflow conditions, these profiles are defined based on earlier studies using LM-6000[4] with appropriate modification to account for the current flow rates. A 7 percent inflow turbulence field is also included in the primary swirl cup flow and a similar initialization is used for the subgrid kinetic energy k_{sgs}.

A Lagrangian-Eulerian approach is used for the two-phase LEMLES whereby, the droplets are tracked in the 3D domain using a Lagrangian technique but when they evaporate, the gas species appears within the subgrid LEM model. Full two-way coupling is employed in these calculations. The methodology used here has been described in the past[28]and therefore, avoided here.

An embedded boundary method is used in this study to resolve the geometry in the inlet and the resolution is fine enough to ensure that the swirling shear layers are well resolved. A total of around 6.7 million grid points (178x258x148) are used to resolve the flow field and typically, around 400,000-800,000 droplet parcels are present (the higher value corresponds to Case 2). A log-normal distribution with a SMD of 50 micron is used for these studies.

4 RESULTS AND DISCUSSION

4.1 Length and Time Scale Resolution

As noted above, in the GLES approach the time and length scales related to the combustion processes are not considered since the flame is modeled as a thin-

surface. However, the turbulent flame speed model used here is not considered valid for high value of u'/S_L. Also, as combustion moves from TRZ to the BRZ regime, the flamelet assumption, on which the G-equation model is based, breaks down. These issues have been investigated earlier[21] and it was shown that GLES approach cannot be used with reliability as the equivalence ratio approaches the LBO limit.

In the LEMLES approach, the length scales from the grid resolution $\overline{\Delta}$ to the Kolmogorov scale η is resolved within LEM, and all processes proceed at their own time scales. Figure 5 shows schematically the length and time scale resolution in the LEMLES for the DOE-HAT case (note that, this is equally true for the GE-1 case). Analysis of the conditions shows that the flame thickness δ_F is resolved at the LES level (Δ_{LES}) and that the reaction zone (δ_{RR}) is resolved at the LEM level. The effect of a typical sub-grid eddy (Δ_{Eddy}) (which is of the order of δ_{RR}) is explicitly included in the sub-grid stirring model in LEM.[8]

The time-scales are also reasonably well resolved. In the current LES, Δt_{LES} is the CFL time-step that is based on the acoustic time scale due to the compressible nature of the simulated flow. The reaction-diffusion equations evolve at the characteristic time step which is a minimum of the diffusion time step, Δt_{diff} and the chemical time step Δt_{chem}. In the current study, $\Delta t_{diff} = \Delta t_{chem}$, and direct integration (using ISAT) is used to evolve the finite-rate kinetics. Δ_{stir} is stirring time interval which decreases with increase in u' and as a result, a large number of stirring events occur in regions of high u' (e.g., shear layer).

4.2 DOE-HAT Premixed Combustion

In the GLES approach, the G-equation model is used to locate the flame front and thus, to obtain the proper heat release without simulating a multi-species flow. In contrast, in the LEMLES approach, when a finite-rate mechanism is employed inside the LEM, the turbulent reaction rates are *predicted* rather than *modeled* (as in GLES), and thus, remains valid.

Figure 6 shows the flame surface and CO and UHC mass fraction. The CO mass fraction isolines follow UHC mass fraction isolines, thus demonstrating that UHC is not a negligible source of CO. The flame surface is wrinkled by the high turbulence in the shear region and is highly compact due to the high swirl and the recirculation zones created downstream of the dump plane that stabilizes the flame.

The GLES model's S_T equation can be manipulated to predict any flame speed even if it is not realistic. In fact, the "bending" of the turbulent flame speed in the TRZ regime can be reproduced in the GLES flame speed model by simplify modifying the constant β. Turbulent flame lengths can be changed by a factor of two or more by model adjustment. The residence time is a direct function of the flame length, and so, the larger the flame length, the smaller is the post-flame residence time. As shown in Fig. 7 maximum CO mass fraction and the shape of the curve can be drastically changed by model manipulation. However, such ad hoc changes are not physical since the flame thickness becomes very large (of the order of the centimeter) and the thin-flame assumption is violated.

In the LEMLES simulation, the flame speed is not modeled and the flame length can not be modified. This is consistent with the fact that in a real gas turbine combustor, the operating conditions vary over a wide range of u'/S_L and ad hoc changes to the flame speed cannot be employed (especially when the flame is transitioning into the BRZ regime). In LEMLES, no special consideration is needed since the local flame speed is resolved in the subgrid as long as the finite-rate kinetics is accurate enough to predict S_L.

Figure 8 compares the CO emission prediction using GLES and LEMLES with and without the inclusion of UHC (a model for local flame quenching is employed here[29]). Without including UHC formation (due to local quenching) the prediction of both methods deviate from data as the equivalence ratio is reduced and the operating conditions approach LBO. Near LBO local quenching is expected which would release UHC into the post-flame zone that will then be oxidized into CO. It is seen that the prediction of CO near LBO improves when UHC is modeled, but the prediction is still lower than the data. This is related primarily to the model (which was originally developed for steady-state quenching[29]) used for the UHC model employed in these studies. However, note that when local extinction occur, the flamelet assumption as well as the models used for emission species.

NO emission is presented in Fig. 9. NO emission prediction is in good agreement with experiments for low equivalence ratio but is under-predicted when Φ increases. Because post-flame mechanisms are responsible of the largest portion of NO emission for Φ>0.5, results suggest that the NO formation rate in the post-flame region is under-predicted. Other factors, like poor macroscopic fuel unmixindness[30] can increase NO formation at the flame front and increase the overall NO emission. In this study, the incoming mixture is assumed to be perfectly premixed and this parameter is not taken into account.

4.3 GE-1 Liquid Spray Combustion

4.3.1 Case 1: Pilot Only (Start-up)

Figures 10(a) and (b) show respectively, the time-averaged temperature profiles at the exit plane of the combustor for Case 1. The radial profile along the center-plane (Fig. 10(a)) and the span-averaged radial profile (Fig. 10(b)) for both the subgrid EBU and LEMLES are shown together for direct comparison. It can be seen that Case 1 shows significant variation in the transverse directions in the temperature profile

since the two pilots are operating in substantially different conditions primarily due to the difference in the physical geometry (the bottom wall is pushing the flow up). Although the center-plane profiles (Fig. 10(a)) show a larger level of unburned fuel and temperature, the span-averaged profiles (Fig. 10(b)) shows a much smoother profiles. Peak temperature in the span-averaged profile is around 750 K although there are distinct peaks close to 800 K in the core of the two pilots.

Figures 11(a) and (b) show respectively, the corresponding radial profiles at the exit plane of the unburned fuel species mass fraction. There is still some unburned fuel at the exit but the level is quite low. The span averaged profiles are more uniform than the center plane. The spanwise variation of the temperature and the unburned fuel at the exit plan (even in an averaged sense) shows that there is significant three-dimensionality in the outflow.

Comparison of the EBULES and LEMLES results show similar results for the current 1-step mechanism. In general, LEMLES predicts a slightly lower temperature and more UHC at the exit plane but the differences are not severe. Although this suggests no specific advantage for the LEMLES, it also not surprising since the 1-step mechanism is primarily providing the global heat release. It remains to be demonstrated that the LEMLES can predict emission better than EBULES.

Figures 12(a) and (b) show respectively, the instantaneous snapshot of the temperature contours in the center plane of the combustor for the EBULES and LEMLES cases. Figures 13(a) and (b) show respectively, the instantaneous snapshot of the temperature contours in the exit plane of the combustor for the EBULES and LEMLES cases. These instantaneous snapshots show typical picture of the burning zone. It can be seen that the LEMLES shows a much compact burning region when compared to the EBULES. EBULES shows pockets of high temperature zones far downstream of the dump plane. These regions are likely to suspect due to the artifact of the EBU model. The exit plane contours also show differences. The EBULES shows pockets of high temperature zones whereas, the LEMLES shows a more distributed and uniform temperature field.

Figures 14(a) and (b) show respectively, the time-averaged contours of the unburned fuel mass fraction in the center plane of the combustor for the EBULES and the LEMLES cases. Figures 15(a) and (b) show respectively, the time-averaged contours of the temperature in the center plane of the combustor for the EBULES and the LEMLES cases. These figures are obtained by averaging over 2 flow through times and show results that are consistent with the instantaneous images. Unburned fuel is distributed over a wider region and at higher concentration for the EBULES when compared to the LEMLES. The time-averaged temperature field also shows a more diffuse field when compared to the LEMLES results.

Finally, Figs. 16(a) and (b) show respectively, the time-averaged contours of the axial velocity contours in the center plane of the combustor for the EBULES and the LEMLES cases. The darkest contour indicates the boundary of the recirculation zones in the two-cups. There are multiple regions of recirculation suggesting that the flame is being stabilized at many scales.

Since there is no data for direct comparison for this test case (although the conditions are realistic) it is difficult to judge the accuracy of these simulations. More detailed analysis is still needed to understand the complex physics of this flow field. However, it is worth noting it is now becoming feasible to carry out such simulations to understand this type of flow field.

4.3.2 Case 2: Pilot+Main (Full Power)

Only limited results for the Case 2 have been obtained so far due to the computational cost involved. For case 2 there is large increase in fuel flow rate which in turn increases the number of droplets that must be injected. Around 800,000 droplets are present in the domain and is injected not only from the pilot region but also from numerous holes along the outer regions.

Figures 17(a) and (b) show respectively, the time-averaged unburned fuel mass fraction and temperature profiles at the exit plane obtained using the EBULES case. Both the center plane and span-averaged profiles are shown for comparison. Again, the span-averaged profiles are smoother when compared to the center-plane profiles. Combustion is actually more efficient in this case since the peak level of the unburned fuel mass fraction is actually an order of magnitude lower than for Case 1.

Figures 18(a)-(c) show respectively, the time-averaged contours of the unburned fuel, temperature and axial velocity in the center plane of the combustor for Case 2. It can be seen with comparison to Case 1 that the unburned fuel exits only in a smaller region closer to the injectors and that the temperature field is much more uniform. Multiple small-scale recirculation regions are present and seem to provide multiple regions for flame holding.

5 CONCLUSIONS

Combustion dynamics near LBO is studied in both premixed and liquid fueled gas turbine engines. In the premixed system, it is shown that although a thin-flame model is computationally efficient it is not applicable near LBO since the flame is in the BRZ regime where there is no thin-flame structure. A subgrid LEM approach is demonstrated to have a ability to deal with flames in all combustion regimes without requiring ad hoc adjustments. It is also shown that oxidation of

UHC in the post-flame zone and local quenching have to be included to obtain the proper CO emission trend (as observed in data) near LBO. Preliminary results in a full-scale liquid-fueled gas turbine are also discussed for a full-scale GE engine. Impact of pilot only and pilot with secondary spray injection is studied to understand the dynamics of interactions between multiple combustor cups. Preliminary results show that present LEMLES approach has the potential for dealing with both premixed and liquid-fueled combustion system without requiring any model adjustments. The accuracy of the LEMLES over EBULES still remains to be demonstrated since comparison with data has not been possible so far in the current GE-1 studies. However, this issue is currently being addressed using the new kerosene-air kinetics and will be reported in the near future.

Acknowledgments

This work was supported by General Electric Aircraft Engine Company.

References

[1] Huan, Y., Hsieh, S. Y., and Yang, V., "Numerical Modeling of Combustion Dynamics of a Lean-Premixed Swirl-Stabilized Injector," *AIAA-02-1009*, 2002.

[2] Kendrick, D. W., Bhargave, A., B., C. M., Sowa, A. W., Maloney, D. J., and Casleton, K. H., "NOx Scaling Characteristics For Industrial Gas Turbine Fuel Injectors," *ASME-2000-GT-98*, 2000.

[3] Mongia, H. C., "Recent Advances in the Development of Combustor Design Tools," *AIAA-03-4495*, 2003.

[4] Kim, W.-W. and Menon, S., "Numerical Simulations of Turbulent Premixed Flames in the Thin-Reaction-Zones Regime," *Combustion Science and Technology*, Vol. 160, 2000, pp. 119–150.

[5] Pitsch, H. and Duchamp De Lageneste, L., "Large-Eddy Simulation of Premixed Turbulent Combustion Using a Level-Set Approach," *Twenty-Ninth Symposium (International) on Combustion*, 2002, pp. 2001–2008.

[6] Bédat, B. and Cheng, R. K., "Experimental Study of Premixed Flames in Intense Isotropic Turbulence," *Combustion and Flame*, Vol. 100, 1995, pp. 486–494.

[7] Mansour, M., Peters, N., and Chen, Y., "Investigation of Scalar Mixing in the Thin Reaction Zones Regime using a simultaneous CH-LIF/Rayleigh Laser Technique," *Proceedings of the Combustion Instutute*, Vol. 27, 1998, pp. 767–773.

[8] Kerstein, A. R., "Linear-Eddy Modeling of Turbulent Transport. Part 6. Microstructure of Diffusive Scalar Mixing Fields," *Journal of Fluid Mechanics*, Vol. 231, 1991, pp. 361–394.

[9] Menon, S. and Kerstein, A. R., "Stochastic Simulation of the Structure and Propagation Rate of Turbulent Premixed Flames," *Proceedings of the Combustion Institute*, Vol. 24, 1992, pp. 443–450.

[10] Smith, T. and Menon, S., "One-dimensional simulations of freely propagating turbulent premixed flames," *Combustion Science and Technology*, Vol. 128, 1996, pp. 99–130.

[11] Chakravarthy, V. and Menon, S., "Large-Eddy Simulations of Turbulent Premixed Flames in the Flamelet Regime," *Combustion Science and Technology*, Vol. 162, 2000, pp. 1–48.

[12] Sankaran, V. and Menon, S., "The Structure of Premixed Flame in the Thin-Reaction-Zones Regime," *Proceedings of the Combustion Institute*, Vol. 28, 2000, pp. 203–210.

[13] Sankaran, V., Porumbel, I., and Menon, S., "Large-Eddy Simulation of a Single-Cup Gas Turbine Combustor," *AIAA-2003-5083*, 2003.

[14] Kim, W.-W. and Menon, S., "A New Incompressible Solver for Large-Eddy Simulations," *International Journal of Numerical Fluid Mechanics*, Vol. 31, 1999, pp. 983–1017.

[15] Fureby, C. and Möller, S.-I., "Large-Eddy Simulation of Reacting Flows Applied to Bluff Body Stabilized Flames," *AIAA Journal*, Vol. 33, No. 12, 1995, pp. 2339–2347.

[16] Schumann, U., "Subgrid Scale Model for Finite Difference Simulations of turbulent Flows in Plane Channels and Annuli," *Journal of Computational Physics*, Vol. 18, 1975, pp. 376–404.

[17] Menon, S. and Kim, W.-W., "High Reynolds Number Flow Simulations Using the Localized Dynamic Subgrid-Scale Model," *AIAA-96-0425*, 1996.

[18] Kim, W.-W., Menon, S., and Mongia, H. C., "Large-Eddy Simulation of a Gas Turbine Combustor Flow," *Combustion Science and Technology*, Vol. 143, 1999, pp. 25–62.

[19] Kerstein, A. R., "Linear-Eddy Model of Turbulent Transport II," *Combustion and Flame*, Vol. 75, 1989, pp. 397–413.

[20] Pope, S. B., "PDF Methods for Turbulent Reactive Flows," *Progress in Energy and Combustion Science*, 1985, pp. 119–192.

[21] Eggenspieler, G. and Menon, S., "Finite Rate Chemistry Modeling for Pollutant Emission Prediction near Lean Blow Out," *AIAA-2003-4941*, 2003.

[22] Peters, N., *Turbulent Combustion*, Cambridge Monographs on Mechanics, 2000.

[23] Westbrook, C. K. and Dryer, F. L., "Simplified Reaction Mechanisms for the Oxidation of Hydrocarbon Fuels in Flames," *Combustion Science and Technology*, Vol. 27, 1981, pp. 31–43.

[24] Fureby, C., "Large-Eddy Simulation of Combustion Instabilities in a Jet Engine Afterburner Model," *Combustion Science and Technology*, Vol. 161, 2000, pp. 213–243.

[25] Pope, S., "Computationally Efficient implementation of combustion chemistry using in situ adaptive tabulation," *Combustion Theory Modelling*, Vol. 1, 1997, pp. 41–63.

[26] Held, T. J., Mueller, M. A., and Mongia, H. C., "A Data-Driven Model for NO_x, CO and UHC Emissions for a Dry Low Emissions Gas Turbine Combustor," *AIAA-2001-3425*, 2001.

[27] Eggenspieler, G. and Menon, S., "LES of Premixed Combustion and Pollutant Emission in a DOE-HAT Combustor," *AIAA-2003-0309*, 2003.

[28] Sankaran, V. and Menon, S., "LES of Spray Combustion in Swirling Flows," *Journal of Turbulence*, Vol. 3, 2002.

[29] Meneveau, C. and Poinsot, T., "Stretching and Quenching of Flamelets in Premixed Turbulent Combustion," *Combustion and Flame*, Vol. 86, 1991, pp. 311–332.

[30] Fric, T. F., "Effects of Fuel-Air Unmixedness on NOx Emissions," *Journal of Propulsion and Power*, Vol. 9, No. 5, 1993, pp. 708–713.

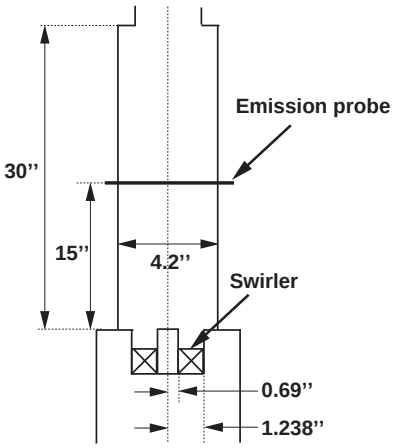

Fig. 2 Geometry and dimensions of the DOE-HAT combustor.

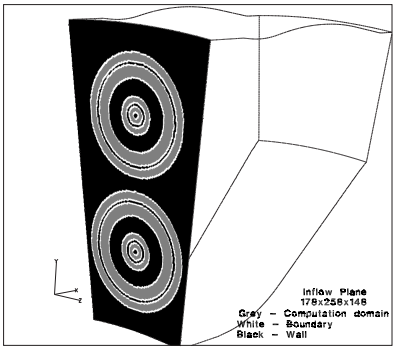

a) Inflow Plane

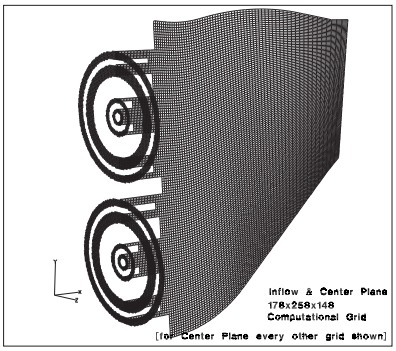

b) Computational Grid

Fig. 3 GE-1 geoemtry and computational domain

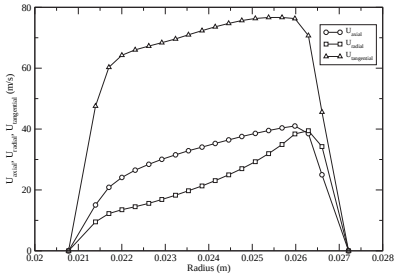

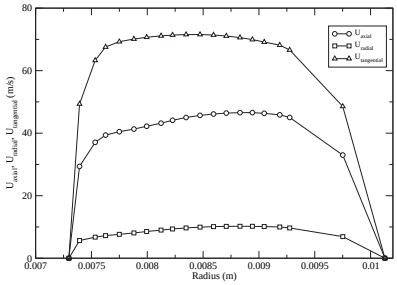

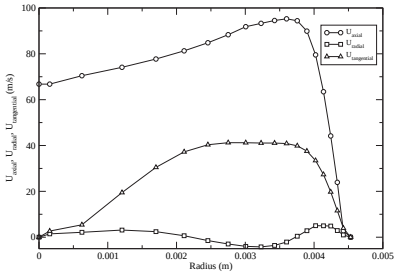

c) Inner

Fig. 4 Inflow profiles used for the GE-1 combustor in each swirl cup. Fully developed parabolic profiles are employed for the outer cooling air circular slots.

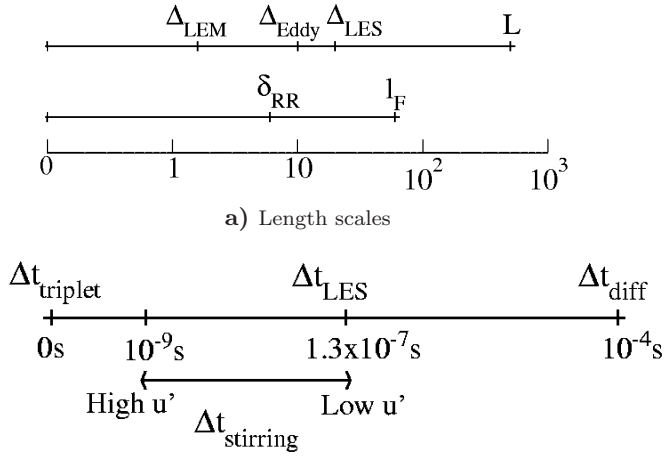

a) Length scales

b) Times scales

Fig. 5 Length and time scale resolution for Φ=0.41 in the DOE-HAT.

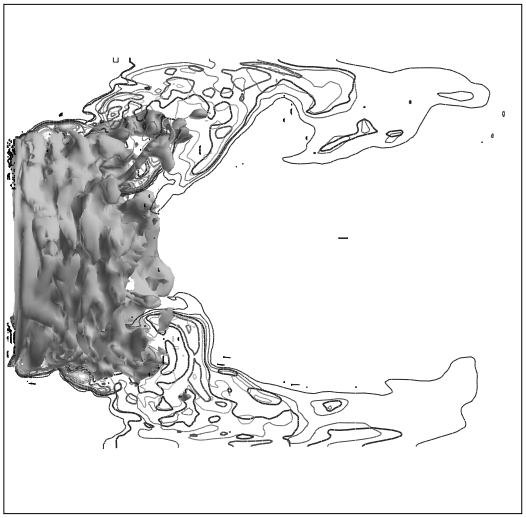

Fig. 6 Instantaneous snapshot of the flame surface, Y_{UHC} isolines (thick contours) and Y_{CO} isolines (thin contours).

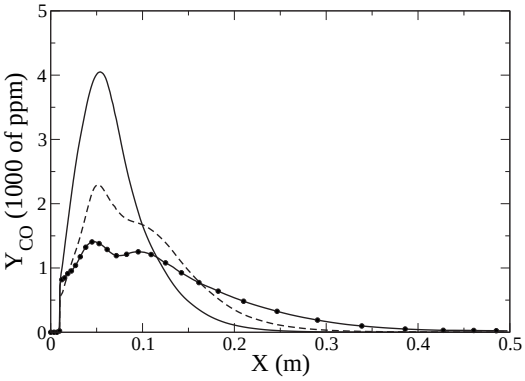

Fig. 7 Influence of the flame speed model upon the CO mass fraction. X is the distance from the combustion chamber dump plane. (— : β=20.0, ζ = 16.56, - - : β=10.0, ζ = 10.00, -•- : β=7.0, ζ = 10.00). Here $\zeta = u'/S_L$.

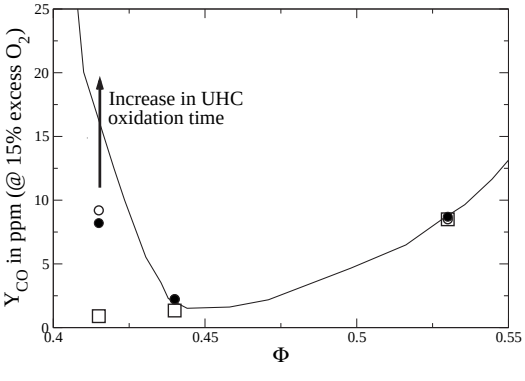

Fig. 8 Experimental and numerical CO emission for different equivalence ratio (— Experiments, •: LEMLES with UHC, □: GLES without UHC, ○: GLES with UHC).

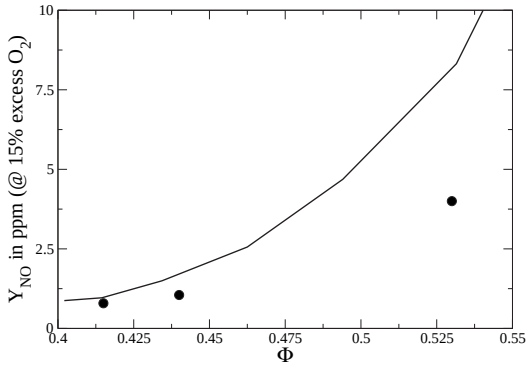

Fig. 9 Experimental and numerical NO emission for different equivalence ratio(— Experiments, •: LEMLES and GLES).

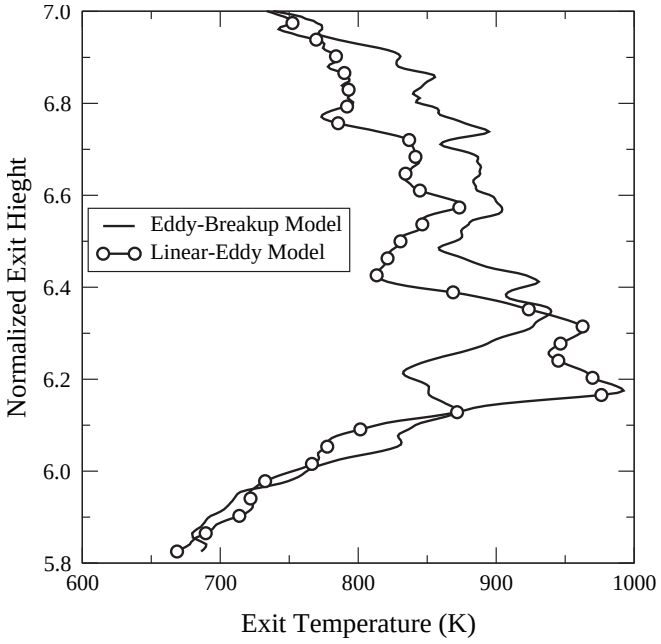

a) Center plane

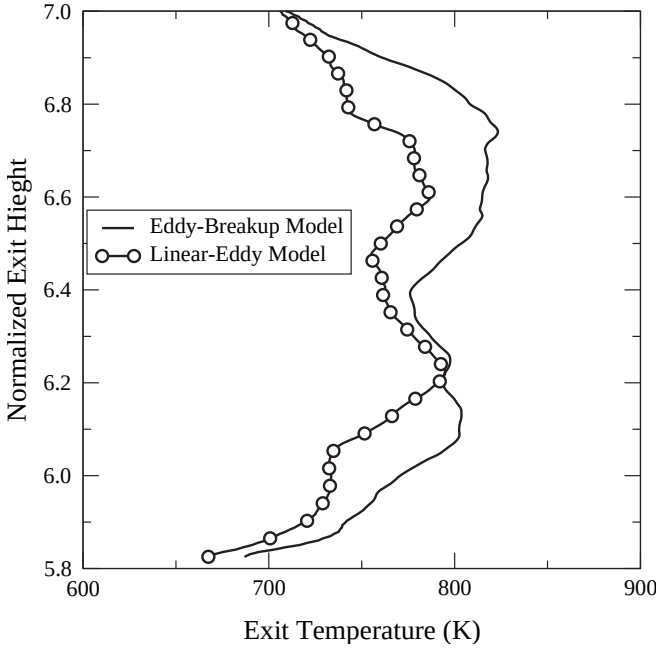

b) Span-averaged

Fig. 10 GE-1 Case 1 time-averaged temperature profiles at the exit plane.

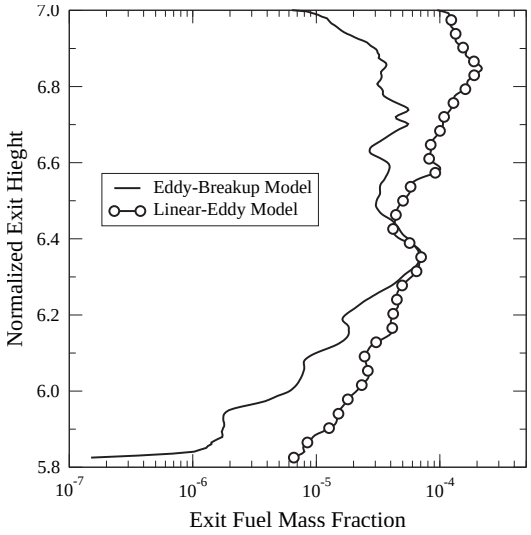

a) Center plane

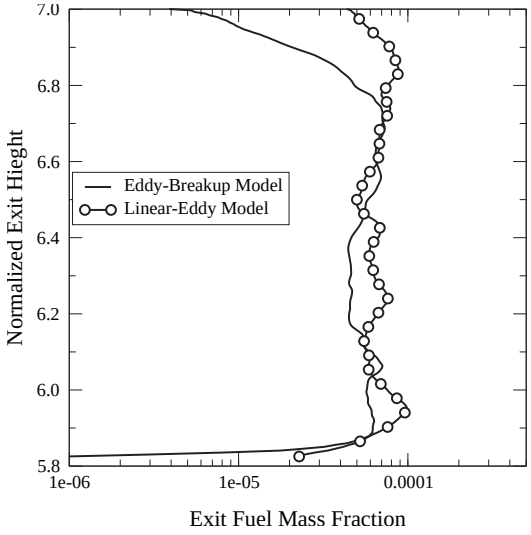

b) Span-averaged

Fig. 11 GE-1 Case 1 time-averaged unburned fuel mass fraction profiles at the exit plane.

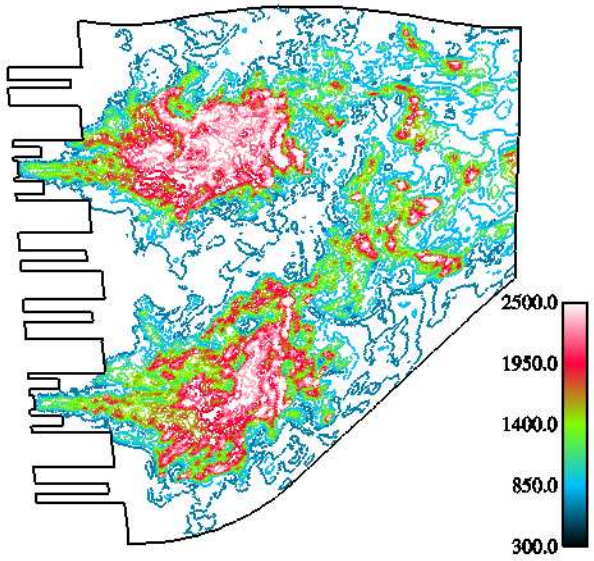

a) Subgrid EBU Prediction

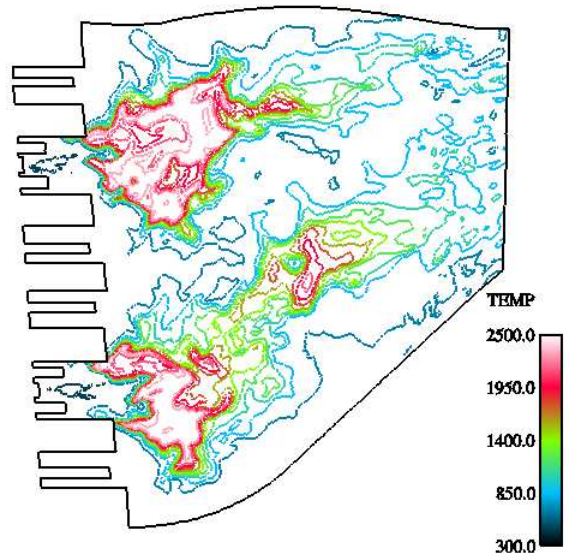

b) Subgrid LEM Prediction

Fig. 12 GE-1 Case 1 Instantaneous center plane temperature contours.

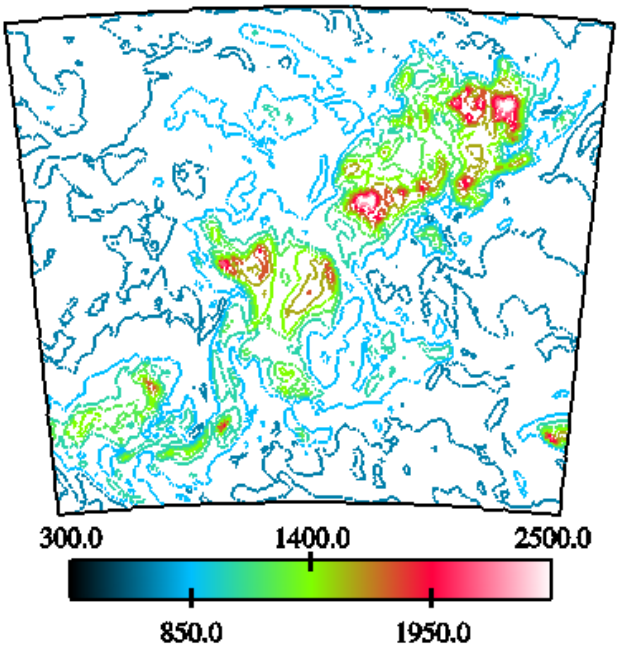

a) Subgrid EBU Prediction

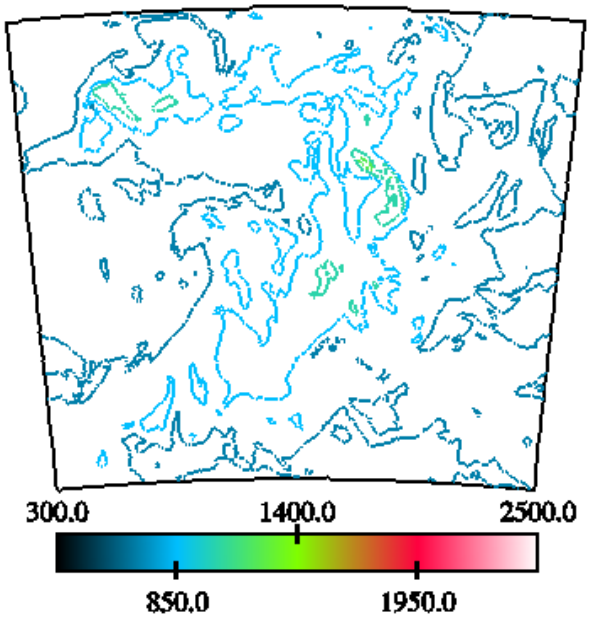

b) Subgrid LEM Prediction

Fig. 13 GE-1 Case 1 Instantaneous exit plane temperature contours.

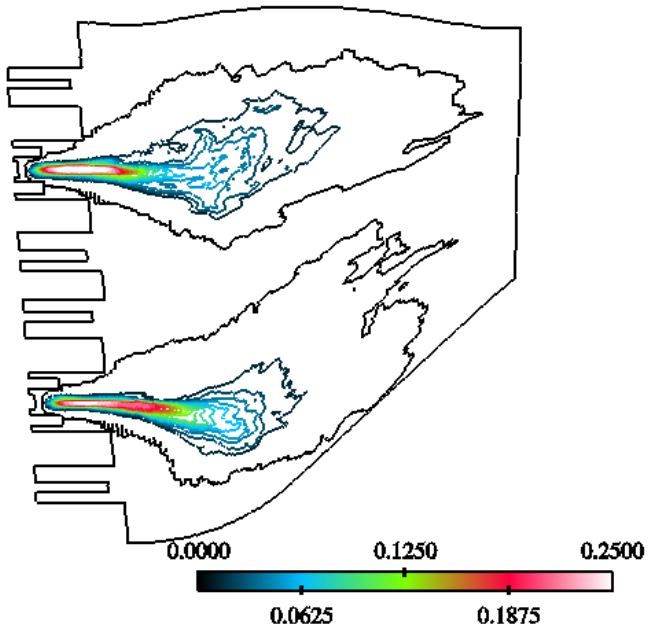

a) Subgrid EBU Prediction

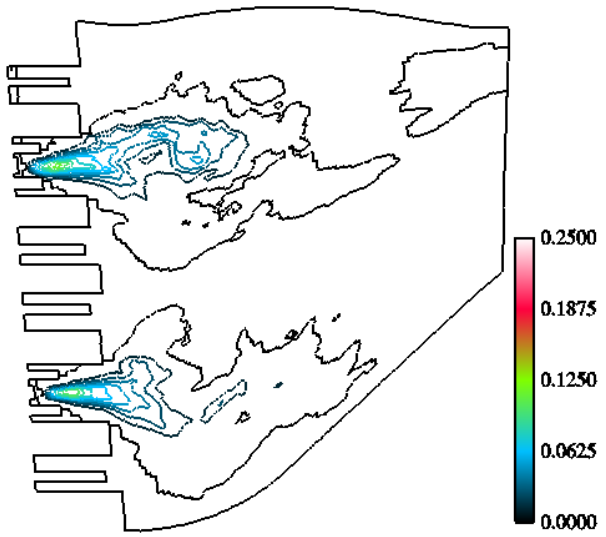

b) Subgrid LEM Prediction

Fig. 14 GE-1 Case 1 time-averaged center plane fuel mass fraction contours.

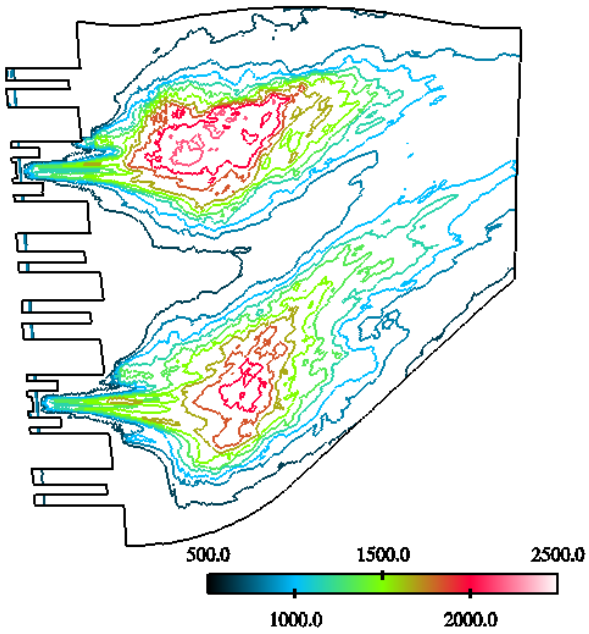

a) Subgrid EBU Prediction

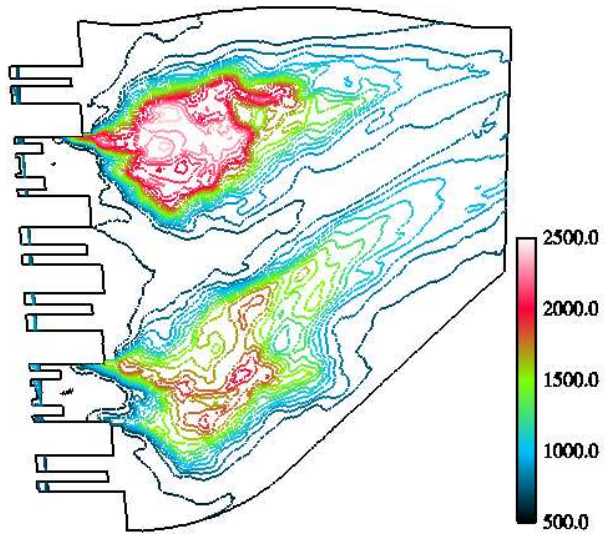

b) Subgrid LEM Prediction

Fig. 15 GE-1 Case 1 time-averaged center plane temperature contours.

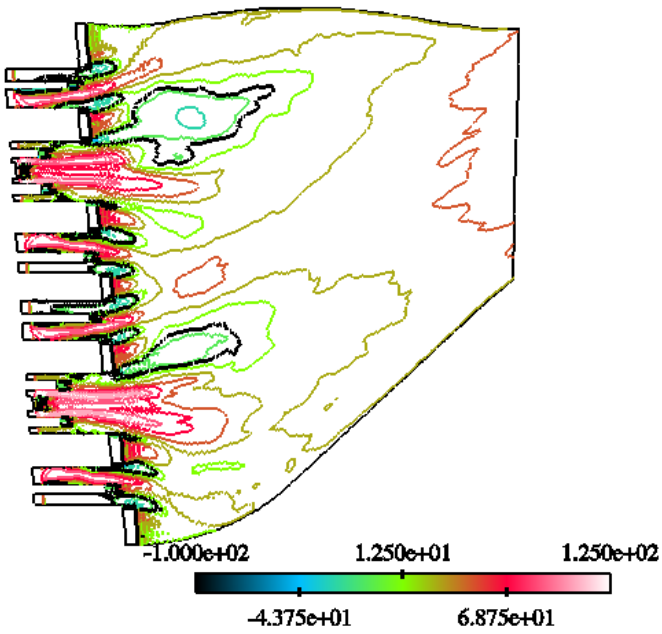

a) Subgrid EBU Prediction

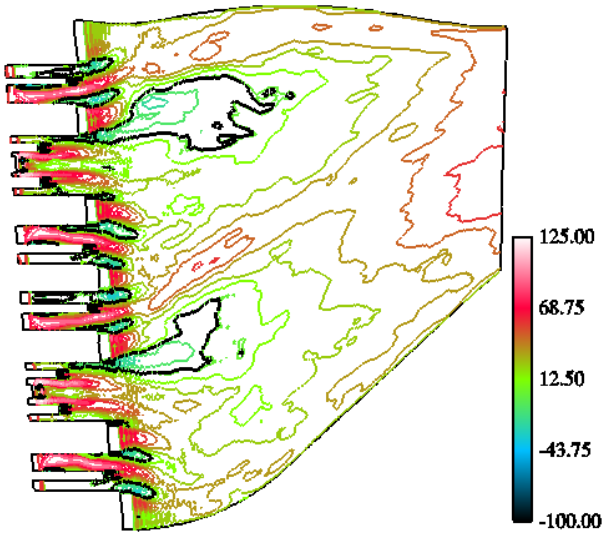

b) Subgrid LEM Prediction

Fig. 16 GE-1 Case 1 time-averaged center plane axial velocity contours.

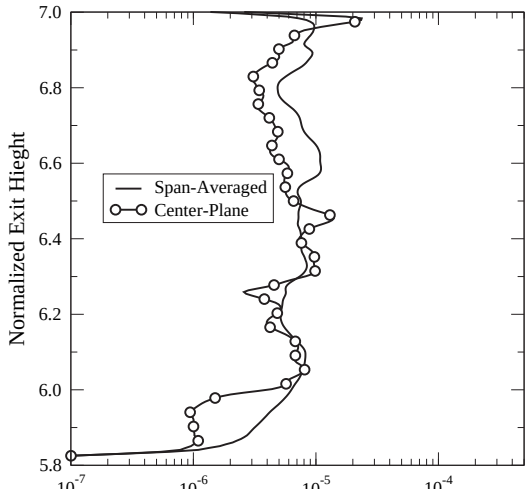

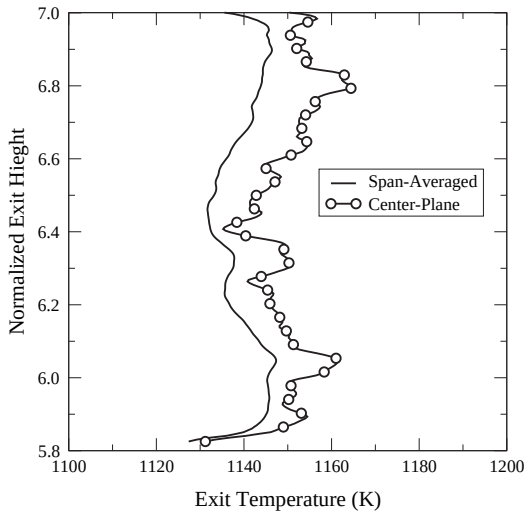

b) Temperature

Fig. 17 GE-1 Case 2 time-averaged center plane and span-averaged exit profiles.

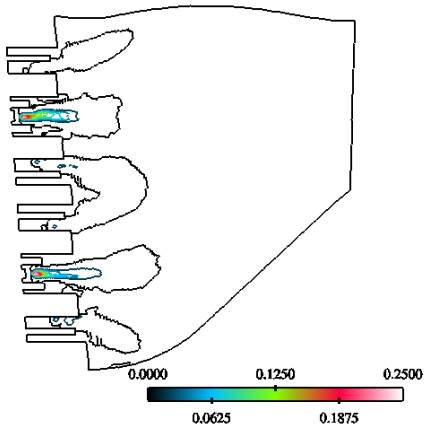

a) Unburned Fuel

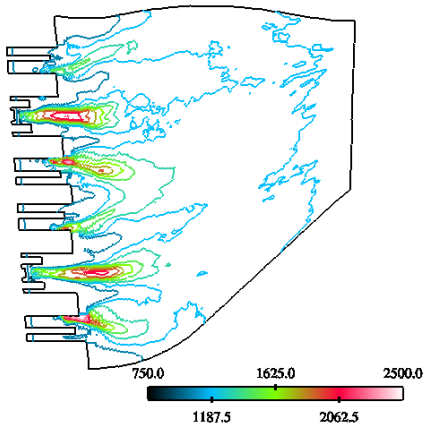

b) Temperature

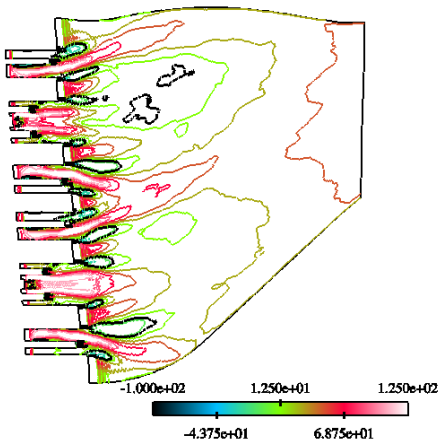

c) Axial Velocity

Fig. 18 GE-1 Case 2 time-averaged center plane contours.